Improved forecasts of winter weather extremes over midlatitudes with extra Arctic observations

Kazutoshi Sato[1], Jun Inoue[1,2,3], Akira Yamazaki[2], Joo-Hong Kim[4], Marion Maturilli[5], Klaus Dethloff[5], Stephen R. Hudson[6], and Mats A. Granskog[6]

[1]National Institute of Polar Research, Tachikawa, Japan, [2]Application Laboratory, Japan Agency for Marine-Earth Science and Technology, Yokohama, Japan, [3]SOKENDAI (Graduate University for Advanced Studies), Hayama, Japan, [4]Korea Polar Research Institute, Incheon, Korea, [5]Alfred Wegener Institute, Helmholtz Centre for Polar and Marine Research, Potsdam, Germany, [6]Norwegian Polar Institute, Tromsø, Norway

Abstract Recent cold winter extremes over Eurasia and North America have been considered to be a consequence of a warming Arctic. More accurate weather forecasts are required to reduce human and socioeconomic damages associated with severe winters. However, the sparse observing network over the Arctic brings errors in initializing a weather prediction model, which might impact accuracy of prediction results at midlatitudes. Here we show that additional Arctic radiosonde observations from the Norwegian young sea ICE expedition (N-ICE2015) drifting ice camps and existing land stations during winter improved forecast skill and reduced uncertainties of weather extremes at midlatitudes of the Northern Hemisphere. For two winter storms over East Asia and North America in February 2015, ensemble forecast experiments were performed with initial conditions taken from an ensemble atmospheric reanalysis in which the observation data were assimilated. The observations reduced errors in initial conditions in the upper troposphere over the Arctic region, yielding more precise prediction of the locations and strengths of upper troughs and surface synoptic disturbances. Errors and uncertainties of predicted upper troughs at midlatitudes would be brought with upper level high potential vorticity (PV) intruding southward from the observed Arctic region. This is because the PV contained a "signal" of the additional Arctic observations as it moved along an isentropic surface. This suggests that a coordinated sustainable Arctic observing network would be effective not only for regional weather services but also for reducing weather risks in locations distant from the Arctic.

1. Introduction

In several recent winters, East Asia and North America have experienced extreme winter weather events with low temperatures and heavy snowfalls. It has been proposed that cold extremes over the midlatitudes are linked to Arctic warming associated with substantial Arctic sea-ice reduction in winter during the last decade [e.g., *Vihma*, 2014; *Cohen et al.*, 2014; *Kim et al.*, 2014; *Overland et al.*, 2015; *Simmonds*, 2015]. Sea ice reduction over the Barents Sea induces anomalous surface heat fluxes [*Honda et al.*, 2009] and changes in cyclone tracks over Eurasia [*Inoue et al.*, 2012], leading to atmospheric variability that causes cold conditions across East Asia. Similarly, it has been asserted that wintertime low temperature over North America is the result of more frequent blocks and/or southward shifts of the jet stream [*Francis and Vavrus*, 2012, 2015; *Overland*, 2016], associated with a decline in sea-ice extent over the Bering Sea [*Lee et al.*, 2015]. *Kug et al.* [2015] stated that extreme winter events over Eurasia and North America are induced by sea ice retreat across the Barents and Chukchi seas, respectively. The decline in Arctic sea ice is also driven by both changes in atmospheric circulation over the Atlantic Ocean [*Sato et al.*, 2014; *Simmonds and Govekar*, 2014; *Luo et al.*, 2016] and water inflows at midlatitudes in the Arctic [*Nakanowatari et al.*, 2014, 2015; *Årthun and Eldevik*, 2016]. Several studies have reported that the extreme cold events over the midlatitudes are induced by changes in tropospheric circulations (e.g., the Arctic Oscillation) [*Liu et al.*, 2012; *Mori et al.*, 2014], with tropical ocean variability as external forcing (e.g., an El Niño event) [*Graf and Zanchettin*, 2012] and a weakened polar vortex in the stratosphere [*Nakamura et al.*, 2015].

Another approach to estimate the impact of Arctic weather conditions on midlatitude weather is an observing system experiment (OSE). The reproducibility of atmospheric circulations over the Arctic region in

reanalysis data, which assimilate observation data (e.g., land-based and satellite) using a data assimilation system, depends not only on model performance [*Inoue et al.*, 2011] but also on the quantity of observations [*Inoue et al.*, 2009, 2013]. Additional data from radiosondes and dropsondes contribute to more accurate reproduction of atmospheric fields [*Kristjánsson et al.*, 2011; *Yamazaki et al.*, 2015], which in turn improve reproducibility and prediction of the Arctic sea ice distribution because of wind-driven sea-ice drift related to the atmospheric circulation [*Ono et al.*, 2016]. Although it has been found through OSEs that radiosonde observation data over the Arctic Ocean significantly improve the analysis ensemble mean and reduce the spread of ensemble members (i.e., uncertainty) in upper tropospheric circulations during summer [*Inoue et al.*, 2013; *Yamazaki et al.*, 2015], their impact on circulations at midlatitudes would be very limited, partly because of the relatively small size of the tropospheric polar vortex during summer.

For winter, studies have focused on the reproduction and prediction skill of forecasting systems for the Arctic through forecast experiments [*Jung and Leutbecher*, 2007; *Jung and Matsueda*, 2014; *Jung et al.*, 2014], but not through data assimilation approaches. Moreover, using relaxation techniques, *Jung et al.* [2014] investigated the Arctic influence on midlatitude weather prediction, suggesting that improvement of initial atmospheric fields over the Arctic enhanced the accuracy of predictions across East Asia and eastern North America. However, those studies did not use OSEs, and so the impact of additional radiosonde observations over the Arctic during winter on weather forecast performance at midlatitudes has not been directly investigated. The large uncertainty in initial conditions over the Arctic might influence forecast skills of atmospheric circulations at midlatitudes, because of stronger westerly jet streams during winter and their meanderings.

Cold-air outbreaks (CAOs) on the east coasts of continents (Eurasia and North America) in the Northern Hemisphere have been substantially investigated [e.g., *Ninomiya*, 1975; *Lenschow and Agee*, 1976; *Dirks et al.*, 1988; *Chou and Zimmerman*, 1989; *Iwasaki et al.*, 2014]. During winter in East Asia, there is typically a strong surface pressure gradient between a developed cyclone over the North Pacific off the coast of Japan and the Siberian high over Eurasia. When a cold air mass passes over the relatively high sea-surface temperature, there is air mass modification [*Inoue et al.*, 2005], resulting in the development of convective clouds that cause extreme weather with heavy snowfall [*Akiyama*, 1981; *Yoshizaki et al.*, 2004]. The same situation is found over the North America. Over the Great Lakes, cold air receives additional heat and moisture, generating cold events with heavy snowfall in the northeastern United States [*Eichenlaub*, 1970]. In general, there is a 500 hPa trough over the Great Lakes region and a ridge over Alaska prior to extreme CAOs [*Konrad*, 1996; *Cellitti et al.*, 2006]. Thus, accurately forecasting extreme cold events is challenging work.

During February 2015, the jet stream frequently meandered over East Asia and eastern North America, causing anomalous low temperatures in these regions (Figure 1). On 9 February, a cold air mass over the Eurasian continent (Figure 1a) resulted in a record maximum daily snowfall and record minimum air temperature at several stations in Japan. In addition, in some areas of eastern North America, the air temperature dropped below $-30°C$ at 850 hPa on 16 February (Figure 1b), freezing portions of the eastern Great Lakes [*Santorelli*, 2015]. Some stations in eastern North America recorded a minimum air temperature for February.

During February 2015, increased radiosonde observations were made on a ship drifting in Arctic sea ice and at several existing operational stations (Figure 2). In the present study, we present the impacts of these additional radiosonde observation data over the Arctic region for forecasting of the CAOs in February 2015 over midlatitudes, using an ensemble data assimilation system and OSEs.

2. Data and Method

2.1. Extra Radiosonde Observations From a Ship and Arctic Stations

The Norwegian young sea ICE expedition (N-ICE2015) was initiated by the Norwegian Polar Institute to understand the impact of the transition to a younger Arctic ice pack on the atmosphere, sea ice, ocean, and ecosystem [*Granskog et al.*, 2016]. During winter and spring 2015, research vessel (RV) Lance was drifting with the ice pack in the area north of Svalbard, obtaining in situ data related to boundary layer meteorology, surface heat budget, ice dynamics, and thermodynamics (the ship track is shown in Figure 2a). During the project, research camps were established on four ice floes (Floe 1: 15 January to 21 February; Floe 2: 24 February to 19 March; Floe 3: 18 April to 5 June; Floe 4: 7 June to 22 June). Three of the camps were established near 83°N, and the last leg was set up near the ice edge [cf. *Granskog et al.*, 2016]. Radiosonde observations (Vaisala RS92) were performed twice daily at 0000 and 1200 UTC during the expedition.
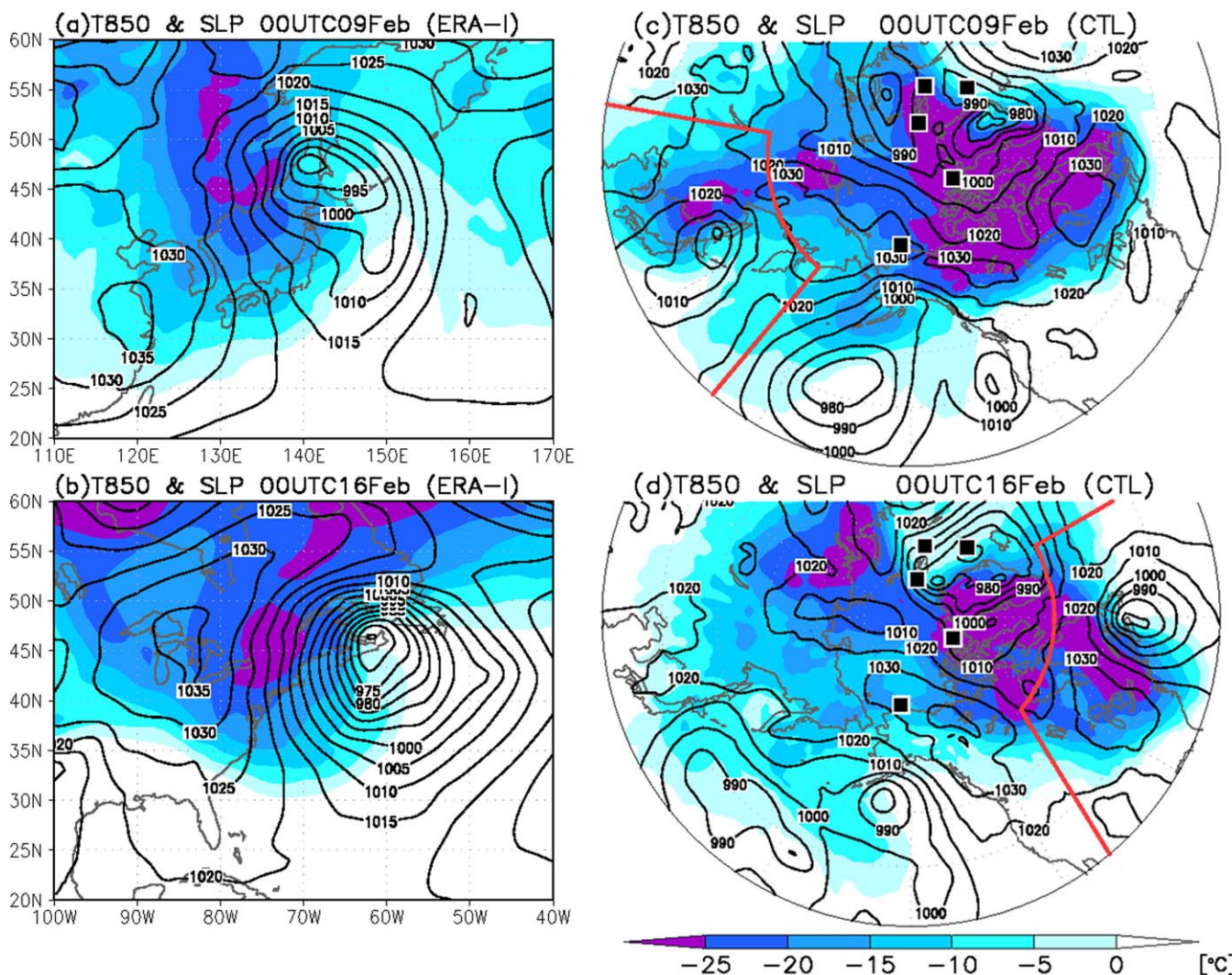
Figure 1. Temperature at 850 hPa (shaded: °C) and sea level pressure (contour: hPa) over (a) East Asia at 0000 UTC 9 February, and (b) eastern North America at 0000 UTC 16 February 2015 in ERA-Interim. The same information in Figures 1c and 1d but for ALERA2 (CTL reanalysis). Areas enclosed by red line correspond to the areas in Figures 1a and 1b. Black squares indicate radiosonde stations shown in Figure 2a.

During the same period as the N-ICE2015 campaign, the daily number of radiosondes was increased at operational land stations (Figure 2b). These stations are the Norwegian stations at Bear Island (74.52°N, 19.02°E) and Jan Mayen (70.93°N, 8.67°W), Canadian station at Eureka (80.0°N, 85.93°W), and American station at Barrow (71.28°N, 156.79°W). Additional observations were made at 0600 and 1800 UTC with the operation, such that radiosonde observations at these stations were mainly done every 6 h (0000, 0600, 1200, and 1800 UTC). The sent data to the Global Telecommunication System (GTS) are shown in Figure 2b. These data were presumed to improve reanalysis products and operational weather forecasts. Figure 3 shows a time-height cross section of potential temperature (PT) obtained by radiosondes during Floe 1 of N-ICE2015. The ice camp was near the center of the tropospheric polar vortex in February 2015 (Figure 2a). A cold dome in the lower troposphere dominated from 6 to 15 February (Figure 3), induced by high potential vorticity (PV) in the upper troposphere.

2.2. Ensemble Reanalysis and Forecasts

We used an ensemble data assimilation system, the so-called ALEDAS2 [*Enomoto et al.*, 2013]. The ALEDAS2 is composed of the Atmospheric general circulation model For the Earth Simulator (AFES) [*Ohfuchi et al.*, 2004; *Enomoto et al.*, 2008] and local ensemble transform Kalman filter (LETKF) [*Hunt et al.*, 2007; *Miyoshi and Yamane*, 2007]. The AFES with horizontal resolution T119 (triangular truncation with truncation wave
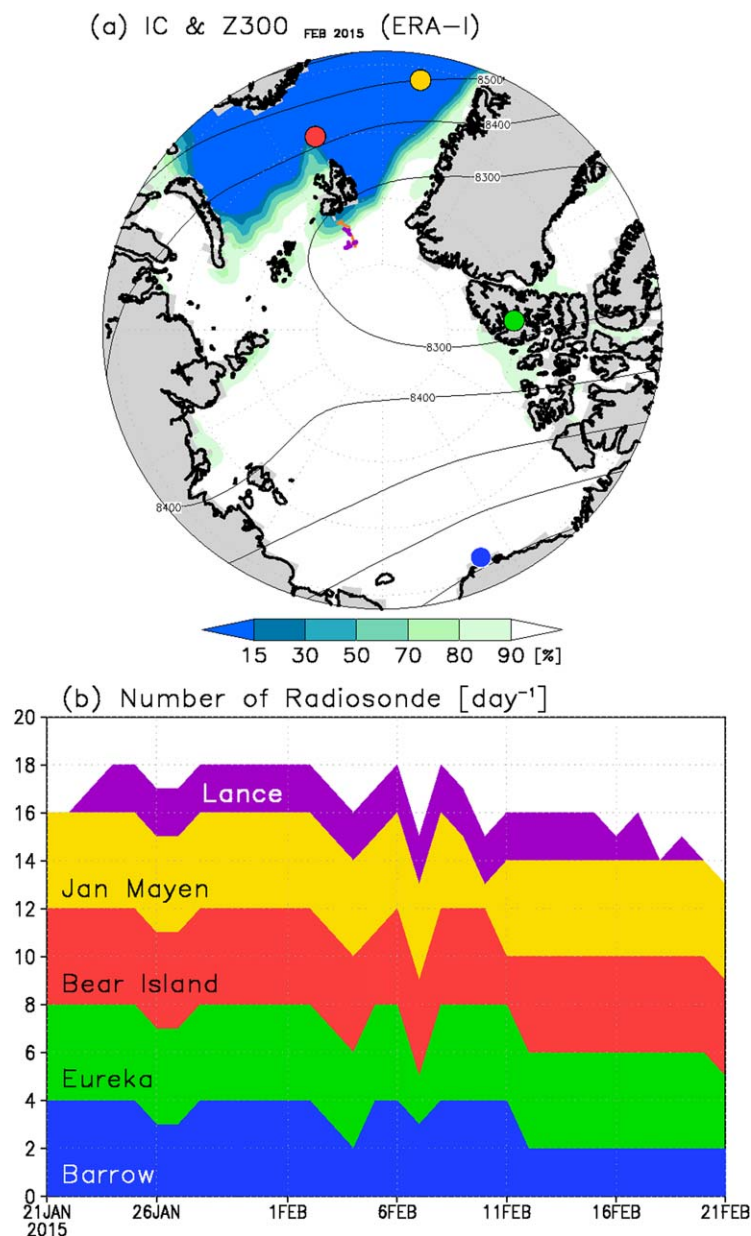
Figure 2. (a) Average sea ice concentration (color shading: %) and geopotential height (contour) at 300 hPa (Z300: m) during February 2015 in ERA-Interim. Color dots indicate radiosonde stations (blue: Barrow; green: Eureka; red: Bear Island; yellow: Jan Mayen). Track and radiosonde observation points of R/V Lance during Floe 1 of N-ICE2015 are shown by orange line and purple dots. (b) Number of daily radiosondes at the stations.

number 119, $\sim 1° \times 1°$) and L48 vertical levels (σ-level, up to ~ 3 hPa) provides 63-member ensemble forecasts. In this study, we can estimate the uncertainty using the spread of the 63 members. National Oceanic and Atmospheric Administration daily 0.25° Optimal Interpolation Sea-Surface Temperature (OISST) version 2 was used for ocean and sea ice boundary conditions [*Reynolds et al.*, 2007]. The AFES-LETKF experimental ensemble reanalysis version 2 (ALERA2) data set is produced with ALEDAS2. It has been shown that ALERA2 reproduces synoptic and large-scale circulations in the troposphere and lower stratosphere as well as other reanalysis products (Figures 1 and 4a–4d) [*Inoue et al.*, 2013; *Yamazaki et al.*, 2015].

The PREPBUFR Global Observation data sets compiled by the National Centers for Environmental Prediction and archived at the University Corporation for Atmospheric Research were used as observation data and were assimilated into the ensemble forecast model using LETKF. We checked that most of the additional observations were included in the PREPBUFER data sets (Figure 2b). Ensemble reanalysis including all PREPBUFR data sets was used as the control reanalysis, i.e., ALERA2 (CTL hereafter). Additionally, an OSE was done to produce an ensemble reanalysis, by excluding all additional radiosonde station data shown in Figure 2 from the PREPBUFR data sets.

To assess the impacts of the additional radiosonde observations at the RV Lance and land-based stations on the prediction of atmospheric circulations, two sets of ensemble forecasts (CTLf and OSEf hereafter) were prepared using the two reanalyses (CTL and OSE, respectively) as initial conditions (Figures 5 and 6). In addition, we built these five reanalysis data sets (OSE_B, _Ba, _E, _J, _L) that excluded additional radiosonde observation data at each station (Bear Island, Barrow, Eureka, Jan Mayen, and RV Lance), and conducted other forecast experiments using five reanalysis data sets (Figures S1 and S2). The forecasting experiments used AFES as the forecast model, with 63 ensemble members. The same forecast model named as ALEDAS2
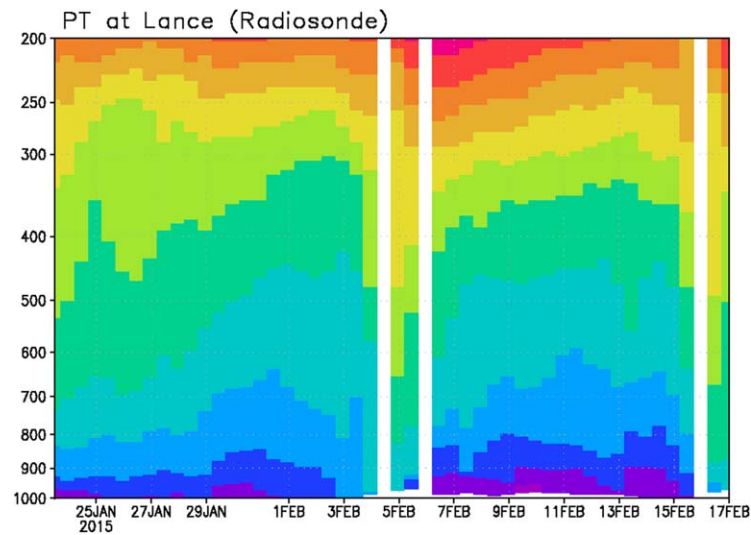
Figure 3. Time-height cross section of potential temperature (PT) (shaded: K) by radiosondes at RV Lance during Floe 1 of N-ICE2015.

were used for all experiments, allowing comparison of forecast results with the ensemble reanalysis (i.e., CTL). In all of these experiments, two integrations over 5.5 days were performed from dates before extreme cold events in East Asia and eastern North America. In the following, most of the results are based on ensemble means. Details of atmospheric fields of target events are given in section 4.

3. Extreme Cold Events at Midlatitudes During Winter 2015

During February 2015, an upper level trough with high PV over the Sea of Japan (Figure 5e) and North America (Figure 6e) generated strong, cold surface circulations across East Asia (Figure 5a) and North America (Figure 6a). On 8 February 2015, a cyclone developed over the Russian coast on the Sea of Japan, with central pressure 995 hPa, and then crossed northern Japan (black track in Figure 5a). The trough at 300 hPa, with a cold core colder than −45°C at 500 hPa, extended to the Sea of Japan (Figure 5e), above the western part of the surface cyclone. This promoted further development of the cyclone and, near the surface, strong cold advection from the continent. The trough with the cold core corresponded to southward intrusion of upper level, high-PV air from the eastern Arctic Ocean, and took less than a week to reach the Far East from the Arctic (Figures 4c and 5e). A cold air mass colder than −10°C at the 850 hPa level reached the main island of Japan on 9 February.
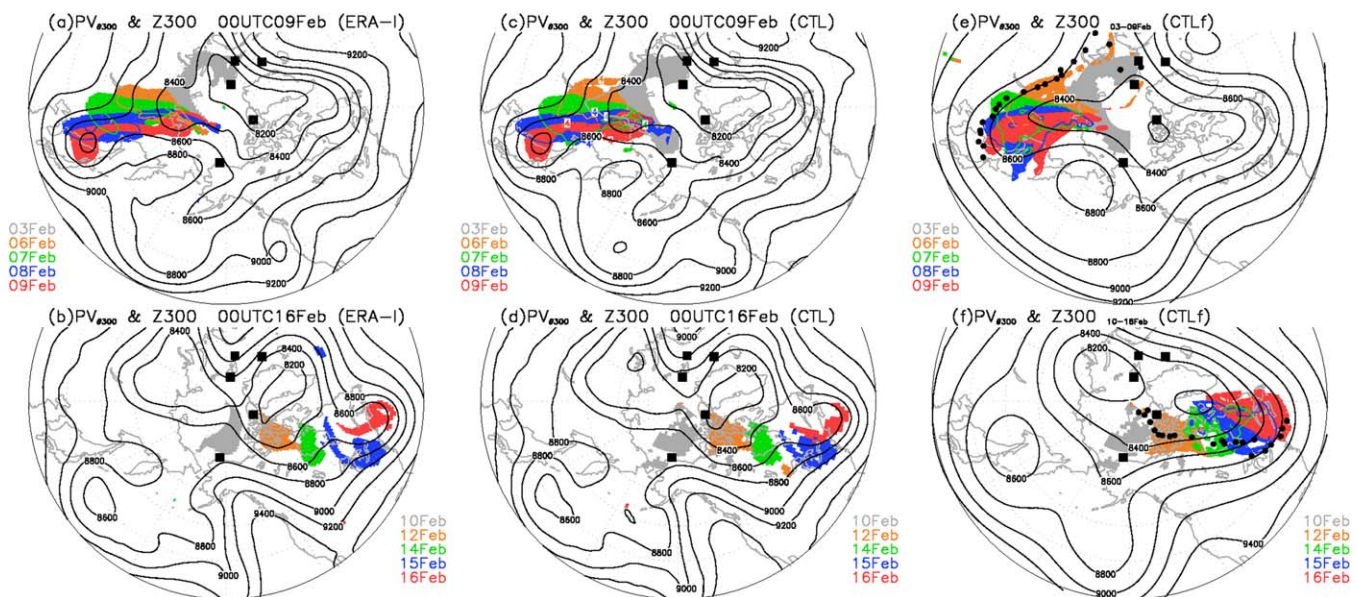

Figure 4. Potential vorticity >4 PVU on 300 K surface at 0000 UTC on each day (color shading: PVU), and geopotential height (contours) at 300 hPa level (Z300: m) at 0000 UTC 09 February (top) and 0000 UTC 16 February (bottom). Some PV fields are masked to highlight temporal evolution of targeted PV. Data are based on (a, b) ERA-Interim reanalysis and (c, d) ALERA2 (control reanalysis: CTL). (e, f) Color shading shows same information in Figures 4c and 4d but for control forecasts (CTLf). Initial date is (e) 3 February and (f) 10 February, respectively. Contours indicate averaged Z300 (m) during forest periods. Black dots in Figures 4e and 4f are trajectories of maximum value point of the difference in Z300 ensemble spread between CTLf and OSEf. Black squares show Arctic observation stations.
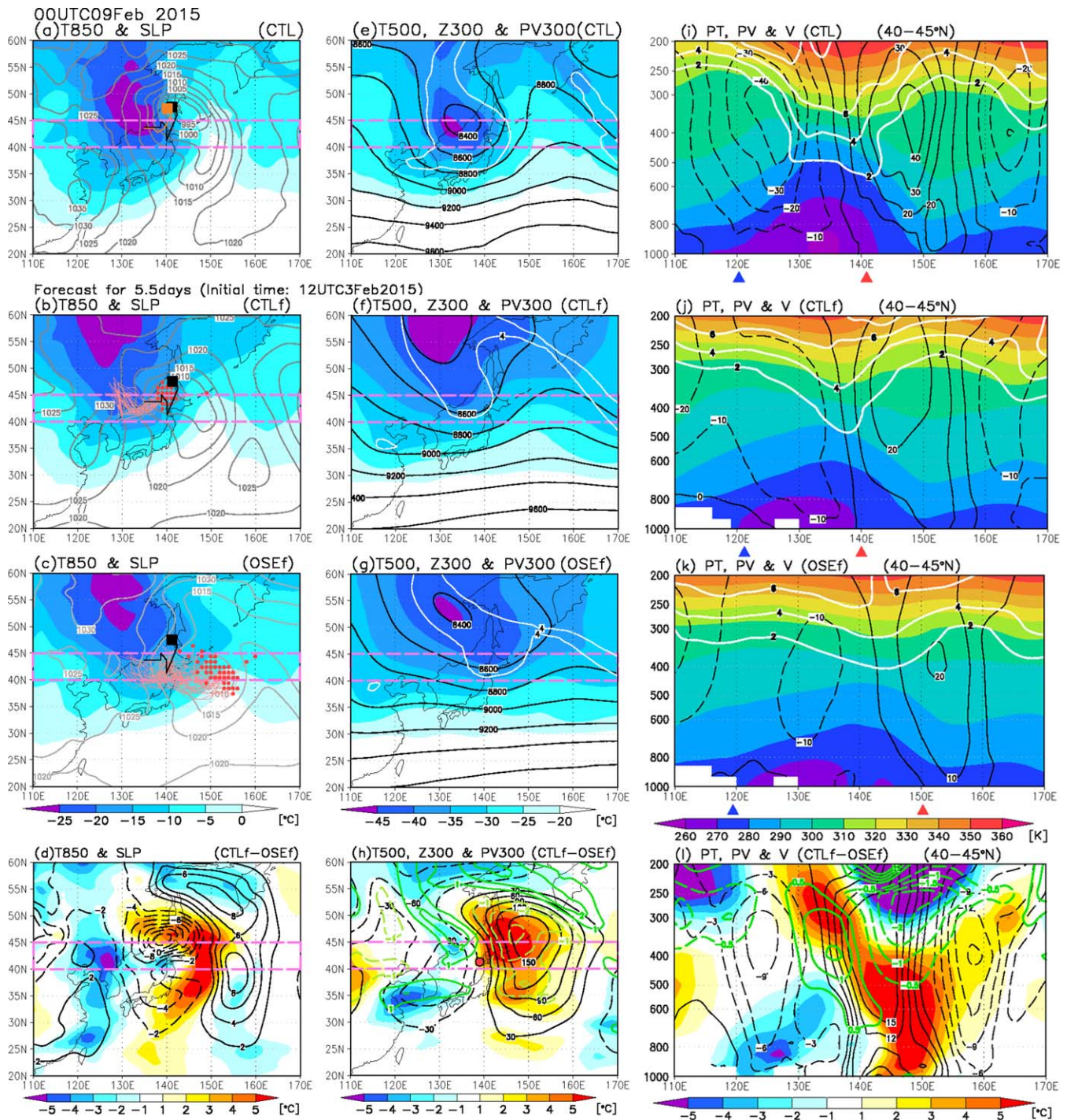
Figure 5. T850 (color shading: °C) and SLP (contours: hPa) at 0000 UTC 9 February 2015 in (a) CTL, (b) CTLf, and (c) OSEf. Difference between CTLf and OSEf is shown in Figure 5d. (e–f) Same as Figures 5a–5d, but for T500 (color shading: °C), Z300 (contours), and PV at 300 hPa (white lines: 4 PVU). Longitude-height cross sections of PV (color shading: K), meridional winds (black contours: m s^{-1}), and PV (white contours: PVU) averaged over areas between 40°N and 45°N (pink lines) shown in Figures 5i–5k; the difference between (j) and (k) is also shown in Figure 5l. Black and orange lines in Figure 5a show track of a cyclone from 1800 UTC 7 February through 0000 UCT 9 February in CTL and ERA-Interim. Red lines in Figures 5b and 5c show track of a cyclone from 1800 UTC 7 February through 0000 UCT 9 February in CTLf and OSEf, for all ensemble members. Red dot in Figure 5h shows maximum value point of difference in ensemble spread of Z300 between CTLf and OSEf (see text for more detail). Red and blue triangles in Figures 5i–5k indicate centers of surface cyclones and anticyclones in CTL, CTLf, and OSEf, respectively.

One week after this event, an extremely cold event with a remarkable meandering of the jet stream occurred over eastern North America (Figures 4d and 6e). An air mass with high PV originated from the Canadian Arctic on 12 February. After crossing the Hudson Bay and Great Lakes, the air mass moved off the
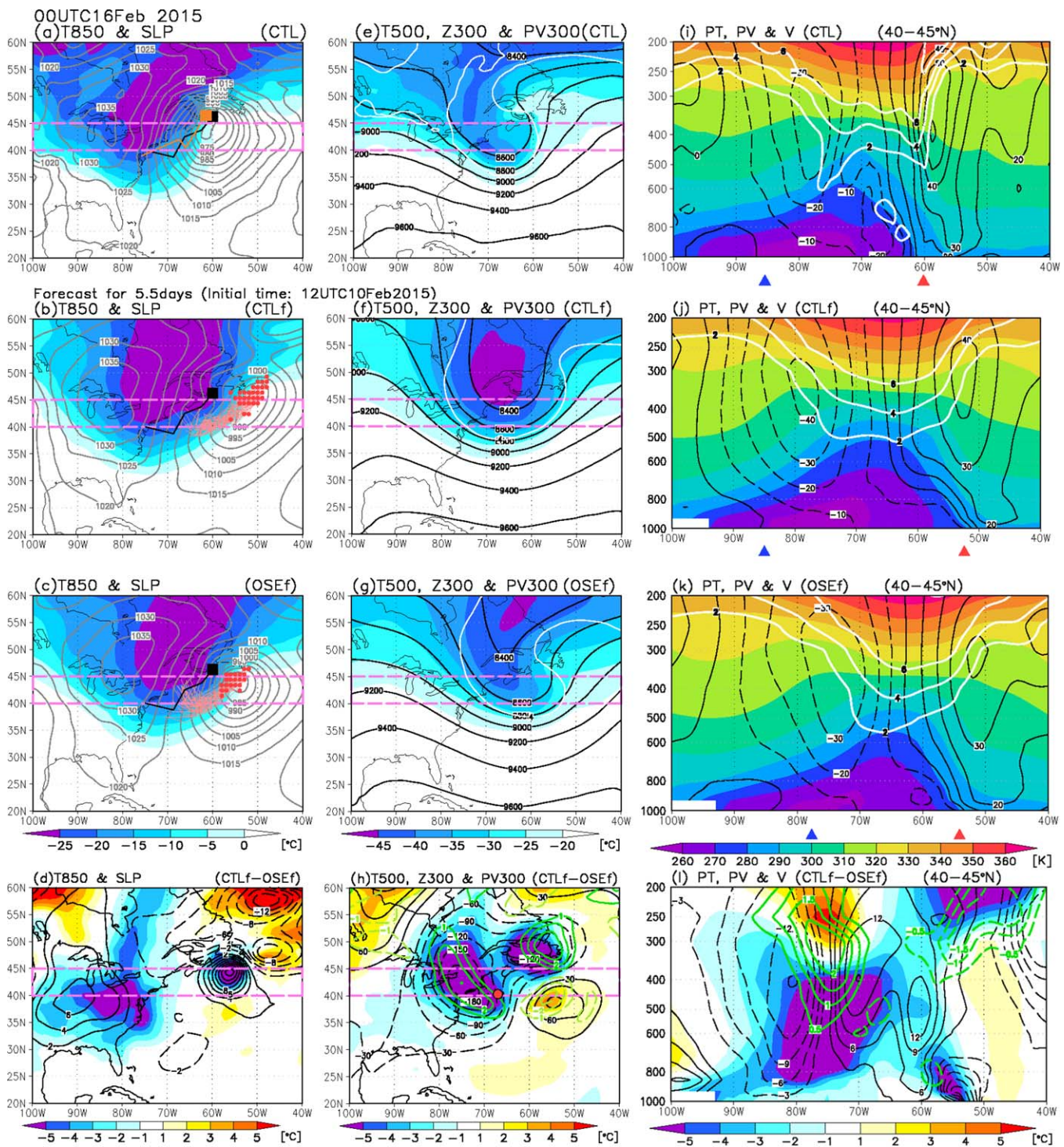
Figure 6. Same as Figure 5 but for North America at 0000 UTC 16 February 2015.

east coast of North America as a trough on 16 February (Figure 4d). The southward intrusion of this high PV influenced the rapid development of a surface cyclone, with minimum central pressure 970 hPa on 16 February (Figure 6a). In addition, a surface anticyclonic circulation (1035 hPa) that dominated the Great Lakes promoted a strong pressure gradient over the east coast of North America. Thus, both the high and low-pressure systems were key factors in determining the cold advection. Minimum temperatures colder than −25°C at the 850 hPa level were found at the eastern edge of the anticyclone.

4. Results

4.1. East Asian Event

Figures 5b and 5f show predicted ensemble mean air temperatures at 850 hPa (T850) and 500 hPa (T500) with sea level pressure (SLP), along with geopotential height at 300 hPa (Z300), for a 5.5 day forecast initialized by ensemble CTL reanalysis on 1200 UTC 3 February. In this CTL forecast (CTLf), a surface cyclone was situated north of Japan (Figure 5b), similar to the result of the ensemble CTL reanalysis (Figure 5a). Northwesterly winds associated with the SLP gradient over the Sea of Japan induced a strong CAO from the continent to Japan. In the upper troposphere, deepening of the trough with high PV at 300 hPa over the Sea of Japan was captured in the CTLf (Figure 5f). These characteristics are similar to the CTL (Figure 5e), suggesting that the CTLf predicted this event well overall.

The same forecast initialized by the OSE (OSEf) produced the results shown in Figures 5c and 5g. The difference in distribution of ensemble mean SLP between CTLf and OSEf was substantial (Figure 5d). To investigate this difference, cyclone tracks using the trajectory of minimum pressure of the cyclone from 1800 UTC 7 February to 0000 UTC 9 February were calculated for the CTL and each member in CTLf and OSEf (tracks in Figures 5a–5c). Ensemble cyclone tracks in the CTLf are very similar to that in CTL, with small spread (Figure 5b), whereas in the OSEf, the locations of ensemble cyclone tracks are far from Japan and widely spread (Figure 5c). This indicates that the cyclone was well predicted in the CTLf but not in the OSEf, resulting in the large difference in ensemble-mean SLP fields (contours in Figure 5d). Thus, the SLP gradient in the CTLf was stronger than in the OSEf over the Sea of Japan, producing a lower temperature pattern in the western part of the cyclone (around Korea; color shading in Figure 5d).

The large difference between the CTLf and OSEf at the upper level trough over the Sea of Okhotsk (Figure 5h) stems from the difference in forecast skills for the trough at 300 hPa, associated with the intrusion of high PV from the Arctic (white contours in Figures 5f and 5g). Anomaly correlation coefficients (ACC) in this area were calculated for the Z300 fields as a measure of this forecast skill (Figure 7a). After 6 February, the ACC remained at 0.8 in the CTLf but suddenly fell to 0.65 in the OSEf, indicating that predictive skill of the CTLf for the trough was higher than that of the OSEf. In addition, the scatter of ACC for the 63 members indicates the degree of uncertainty. The wider range of ACC from 0.4 to 0.9 in the OSEf demonstrates greater forecast uncertainty compared with that of the CTLf.

To address the relationship of the differences of upper level trough and surface cyclone, Figures 5i–5k show longitude-height cross sections of PT, PV, and meridional winds averaged between 40°N and 45°N at 0000 UTC 9 February 2015. The center of the cyclone is around 141°E in the CTL reanalysis (red triangle in Figure 5i). In the western part of the cyclone, lower PT accompanied by northerly winds is observed in the lower and mid troposphere. In the upper troposphere, an increase in PT is found by a tropopause fold from the high-PV intrusion (Figures 4c and 5i). CTLf predicted a cold dome and northerly winds on the western side of the cyclone in the lower and mid troposphere, but the PT is warmer than that in the CTL reanalysis, partly because of weaker PV in the upper troposphere (Figures 5i and 5j). By contrast, the OSEf did not capture the cold dome in the lower and mid troposphere as clearly, nor the warm core in the upper troposphere (Figure 5k), owing to the failure to forecast the high-PV intrusion from the upper troposphere (Figure 5g). Overall, the failure of forecasting the southward intrusion of the high-PV and associated development of the cyclone in the OSEf caused major differences in temperature and wind fields throughout the troposphere (Figure 5l).

Based on these results, errors of predicted surface circulations in the OSEf stem from errors in upper tropospheric circulations, suggesting that the impact of extra radiosondes in the Arctic region on weather forecasts across East Asia would be very strong when there is a high-PV intrusion from the Arctic region to the midlatitudes.

4.2. North American Event

We conducted the same forecast experiments as detailed above, focusing on the cold event in North America on 16 February 2015. The initial time was set to 1200 UTC on 10 February. In contrast to the previous case, neither CTLf nor OSEf captured the development and location of the cyclone over the east coast of North America (Figures 6b and 6c). Comparing the cyclone over Nova Scotia with that in the CTL (black square in Figure 6a), its location in the CTLf and OSEf is further east, off the coast of Newfoundland (Figures 6b and 6c). The deepening and track of the cyclone had similar tendencies in the two forecasts.
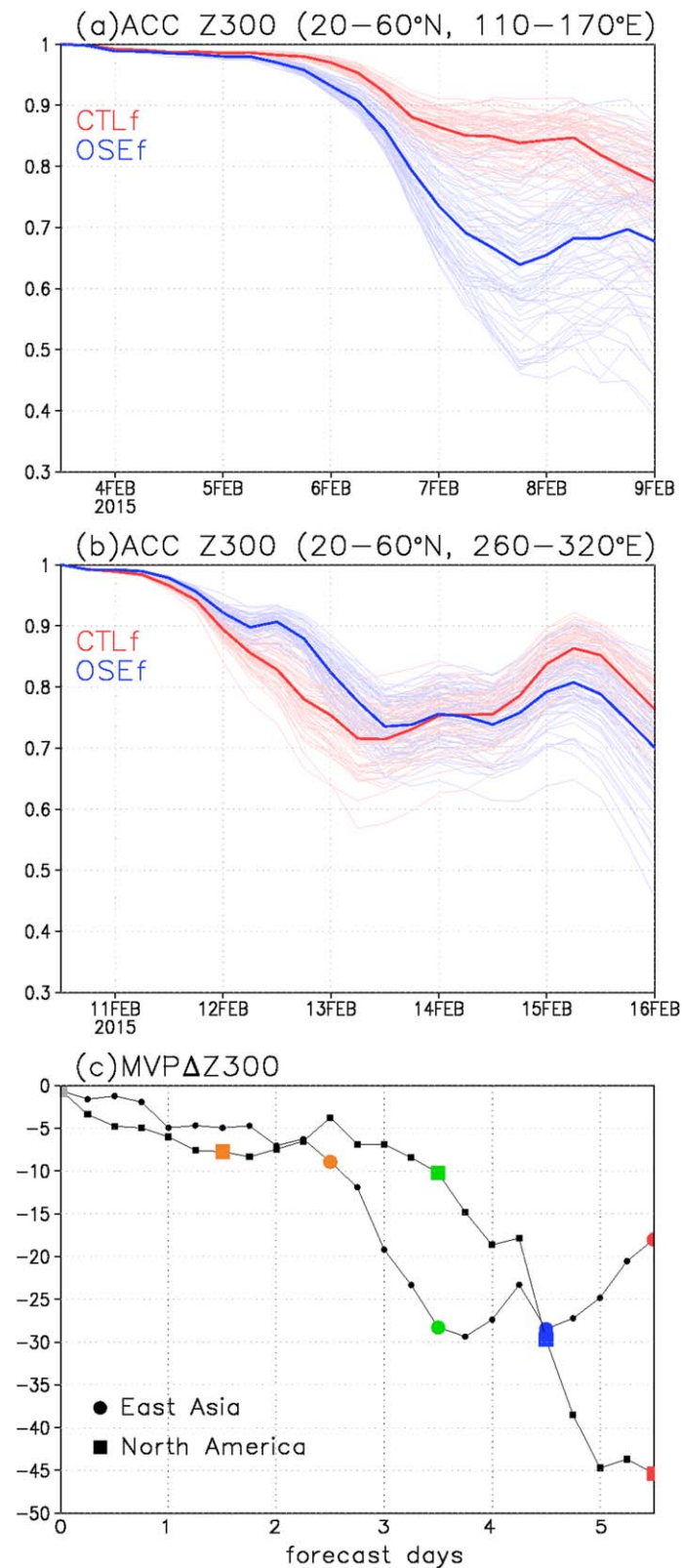
Figure 7. Temporal evolution of anomaly correlation coefficients (ACC) for each ensemble member of CTLf (red lines) and OSEf (blue lines) over (a) East Asia (20°N–60°N, 110°E–170°E) and North America (20°N–60°N, 260°E–320°E) versus CTL reanalysis. Each thick line shows mean value of ACC. (c) Temporal evolution of maximum value point of difference in ensemble spread of Z300 between CTLf and OSEf (MVPΔZ300) for East Asia (closed circles) and North America (closed squares) cases. Color of each mark corresponds to date shown in Figure 4.

However, the difference in predicted T850 between the CTLf and OSEf on 16 February were >5°C over a large area southeast of the Great Lakes and >3°C over Florida (Figure 6d). This discrepancy resulted from a difference in cold advection behind the cyclone. A high-pressure system centered over the Great Lakes was also a major determinant of the cold advection. The center of that system in the CTLf was situated directly over the Great Lakes (1035 hPa; Figure 6b), very similar to the CTL (1035 hPa; Figure 6a). The OSEf had the system northeast of the Great Lakes (Figure 6c). The difference in SLP between the CTLf and OSEf exceeded 6 hPa southwest of the Great Lakes region, producing a T850 difference around the high-pressure system (Figure 6d).

As in the previous case, the additional errors in OSEf appear related to the upper atmospheric circulation. Longitude-height cross sections of PT and meridional winds that averaged between 40°N and 45°N at 0000 UTC 16 February 2015 are shown in Figures 6i–6k. In the CTL, the center of cyclone is around 60°W (Figure 6i). A cold dome (colder than 270 K) is found in the lower and mid troposphere around 63°W–96°W, corresponding to northerly winds at the near surface. The eastern edges of the cold domes in both the CTLf and OSEf are shifted eastward to around 58°W (Figures 6j and 6k) because of the different cyclones positions relative to the CTL (Figure 6i). The difference in PT between the CTLf and OSEf is large below the upper level high-PV air (trough) in the mid and lower troposphere (Figure 6l). The westward elongated tail of the cold dome in the CTLf owes to its better prediction of the location of the surface anticyclone relative to that in the OSEf. The more eastward shift of the high-pressure system in the OSEf is associated with a narrower southward intrusion and more eastward shift of the upper trough (e.g., 8800 m height at 300 hPa in Figures 6e–6g and PV in Figures 6i–6k).

The difference in ACC of Z300 between the CTLf and OSEf was actually very small, with poorer predictive skill than in the previous case (Figure 7b). T850 in the CTL reanalysis over the Great Lakes (Figure 6a) was colder than in the CTLf (Figure 6b), indicating that forecasting this case using AFES and ALERA2 was difficult, even by the CTLf. However, even though the forecast skills were almost the same, the spread of ACCs of the 63 members (i.e., uncertainty) was smaller in CTLf (Figure 7b), implying that the CTLf would be better than the OSEf. Therefore, the continental coldness is more difficult to predict without the extra radiosonde data from the Arctic regions (i.e., OSEf).

5. Summary and Discussion

We focused on the predictability of extreme weather events over East Asia and North America in winter (February) 2015, and its relationship to additional observations in the Arctic. Ensemble forecasts using two ensemble reanalysis data sets, in which additional radiosonde observations from Arctic land-based stations and an ice camp in the drift ice north of Svalbard during N-ICE2015, were either assimilated or excluded. This revealed that continental cold air outbreaks were better predicted in both events if the initial data included the additional observations.

It has been assumed that the sparseness of data over the Arctic is a source of error in reanalysis data and forecasts [e.g., *Inoue et al.*, 2013, 2015], particularly in relation to upper troposphere circulations. Flow-dependent errors tagged by large ensemble spreads at upper levels were expected to be advected with high-PV air along the polar vortex because of strong westerly winds, affecting the reproducibility of the atmospheric circulation at the surface around and below this PV. During summer, the influence of Arctic radiosonde observations would be limited to high latitudes, because of the small spatial scale of the polar vortex and its decreased interaction with lower latitudes [*Inoue et al.*, 2015]. During winter, however, when the horizontal scale of the polar vortex is greater, the additional radiosonde observations can influence much more extensive areas (to the midlatitudes), because of a stronger jet stream and its frequent meanderings.

To understand the origin of the large uncertainties in the upper troposphere at the midlatitudes, we assessed the temporal evolution of the difference in ensemble mean and spread of Z300 between the CTLf and OSEf (ΔZ300), as an indicator of error originating from the "signal," i.e., information for improving ensemble mean state and reducing uncertainty by the additional observations in the Arctic. Although both differences in ensemble mean and ensemble spread of Z300 between the CTLf and OSEf (i.e., error and uncertainty) would be carried and amplified with the increase in lead time, the ensemble mean difference is not a useful parameter as the signal indicator of the additional observations because of large phase errors arisen from the displacement of synoptic disturbances (Figure S3). Instead of that, a maximum value point of ΔZ300 in spread (hereafter MVPΔZ300) at each time was calculated as action centers of ΔZ300 fields (i.e.,

red dots in Figures 5h and 6h). The time evolutions between MVPΔZ300 and ΔZ300 are shown in Figure S4. Figure 7c shows temporal evolution of the MVPΔZ300 (spatial relationships between MVPΔZ300 and ΔZ300 are shown in Figure S4). It remained small ($<$10 m) until forecast days 3 and 4 in the East Asia and North America cases, respectively (Figure 7c). However, it decreased by as much as 30 and 45 m after that in each case, indicating that the difference in uncertainties of Z300 between CTLf and OSEf grew with increasing forecast time. In other words, the impact of extra observations on the forecasts amplified within a few days. In addition, considering that MVPΔZ300 reached target regions (East Asia and North America) for early time in the North America case (Figure S4), the distance between the translating MVPΔZ300 from the Arctic and target regions would be an important determinant of predictable lead time. This is why the ACC in the North America case ($<$0.8) was smaller than in the East Asia case ($>$0.9) for early lead times (e.g., 3 forecast days; Figures 7a and 7b).

The trajectory of MVPΔZ300 during the forecast started in the Arctic region and followed the meandering of the jet stream in each case (dots in Figures 4e and 4f). In the East Asia case, the signal was near Bear Island at the initial time, moved along the trough over Siberia, and finally reached East Asia on 9 February (Figures 4e and 5h). In the North American case, the signal was near station Eureka at the initial time, then traveled from the Canadian Arctic toward eastern North America along the trough over the Canadian Arctic Archipelago (Figures 4f and 6h). The trajectory appeared to be confined by the high-PV area, which moved southeastward and intruded into midlatitudes in each case. It appears as if the PV brought additional errors and uncertainties caused by the lack of the extra observations along upper level isentropic surfaces. Thus, high PV would adiabatically transport errors and uncertainties toward midlatitudes, amplifying forecast errors during the latter forecast period (Figures 7c, S3, and S4). This concept offers new insight into predictability studies of linkages between polar region and midlatitudes.

The aforementioned concept pertains to error propagation from polar to midlatitude regions, but not from observation points. According to the MVPΔZ300 trajectory (Figures 4e and 4f), the large errors and uncertainties over East Asia (North America) appear to originate near Bear Island or Jan Mayen (Eureka or Barrow). However, data from these stations do not always have strong impacts on forecasts. For example, in the East Asia case, OSEf_B (Figure S2b) showed a signal very similar to OSEf (Figure 5d), whereas OSEf_J (Figure S2d) had less impact compared with OSEf. This would stem from "signals" from each observation point that depend on flow within the tropospheric polar vortex, because previous studies have implied that the signal of a single observation is not localized around the observation point but spread under dynamical constraints [*Inoue et al.*, 2013; *Yamazaki et al.*, 2015]. In other words, we still cannot determine where the optimal observation point within the polar vortex is for predicting extreme weathers at the midlatitude. As a possible approach to evaluate the effects of observations from each point individually, Ensemble Forecast Sensitivity to Observations (EFSO) [*Kalnay et al.*, 2012; *Ota et al.*, 2013; *Hotta*, 2014] would be a candidate in an OSE study using ALEDAS2, because EFSO is a diagnostic technique to evaluate impacts of individual observations on global error reduction in a flow-dependent sense to some extent. We are currently in the process of implementing EFSO in ALEDAS2 so that further hints might provide an answer to optimal observation point, using a new ALEDAS2.

Weather in midlatitudes is also influenced by the Tropics (e.g., ENSO). *Jung et al.* [2014] revealed that the Tropics have a stronger influence than the Arctic on the atmosphere in some areas of the Northern Hemisphere, but vice versa for the North Atlantic and North Pacific. The year of polar prediction [*Jung et al.*, 2016] and year of maritime continent from mid-2017 to mid-2019 should provide a great opportunity to explore the roles of polar regions and Tropics on the predictability of weather extremes at midlatitudes.

Appendix A: Reproducibility of Atmospheric Fields in ALERA2 and Calculation Method of MVPΔ300 Trajectories

To assess the reproduction of atmospheric fields in ERA-I and CTL, we compared them using radiosonde observations. The cold dome portrayed by radiosonde data (Figure 3) was well captured by reanalysis data (e.g., ERA-Interim [*Dee et al.*, 2011]; Figure S5a), partly because the radiosonde data from N-ICE2015 and existing land-based stations were sent to the GTS. The tropopause, defined by 2.0 PV units, reached the 400 hPa level from 6 to 16 February 2015 (Figure S5a). As we expected, this tropopause folding corresponding to high lower stratospheric PV in the upper troposphere generated a cold dome in the lower troposphere. The distributions of geopotential height at the 300 hPa level (Z300) in ERA-Interim at 0000 UTC 9 February and 0000

UTC 16 February are shown in Figures 4a and 4b. Meanders of the jet stream occurred during both periods over East Asia and eastern North America, producing severe cold events at midlatitudes (Figures 1a and 1b). Based on the temporal evolution of PV fields on the 300 K surface, a southward intrusion of high PV (color shading in Figures 4a and 4b) influenced cold domes below and the development of cyclones at midlatitudes and associated weather extremes. The CTL reproduced the characteristics of vertical structures of PT and PV (Figures S5a and S5b) and the horizontal distributions of Z300 and PV seen in ERA-Interim (Figures 4a–4d).

The trajectories of the maximum value points of the difference in ensemble spread of Z300 between the CTLf and OSEf (MVPΔZ300) in Figure S4 were calculated as the following procedures. The position of MVPΔZ300 at initial time is defined as the geographical point where the spread differences of Z300 have maximum value close to the target observation stations (Bear Island or Jan Mayen for the East Asia case and Eureka or Barrow for the North America case). The MVPΔZ300 position at the next time step (6 h later) is the point with the maximum spread difference of Z300 closest to the previous MVPΔZ300 position. The same procedures are repeated and thus every MVPΔZ300 position can be traced forwardly. The trajectories are the tracks of the MVPΔZ300 positions from the initial times to 5.5 days after.

References

Akiyama, T. (1981), Time and spatial variations of heavy snowfalls in the Japan Sea coastal region. Part I. Principal time and space variations of precipitation described by EOF, *J. Meteorol. Soc. Jpn.*, *59*, 578–590.

Årthun, M., and T. Eldevik (2016), On anomalous ocean heat transport toward the Arctic and associated climate predictability, *J. Clim.*, *29*, 689–704, doi:10.1175/jcli-d-15-0448.1.

Cellitti, M. P., J. E. Walsh, R. M. Rauber, and D. H. Portis (2006), Extreme cold air outbreaks over the United States, the polar vortex, and the large-scale circulation, *J. Geophys. Res.*, *111*, D02114, doi:10.1029/2005JD006273.

Chou, S.-H., and J. Zimmerman (1989), Bivariate conditional sampling of buoyancy flux during an intense cold-air outbreak, *Boundary Layer Meteorol.*, *46*, 93–112, doi:10.1007/bf00118448.

Cohen, J., et al. (2014), Recent Arctic amplification and extreme midlatitude weather, *Nat. Geosci.*, *7*(9), 627–637.

Dee, D. P., et al. (2011), The ERA-interim reanalysis: Configuration and performance of the data assimilation system, *Q. J. R. Meteorol. Soc.*, *137*, 553–597, doi:10.1002/qj.828.

Dirks, R. A., J. P. Küettner, and J. A. Moore (1988), Genesis of Atlantic Lows Experiment (GALE): An overview, *Bull. Am. Meteorol. Soc.*, *69*, 148–160, doi:10.1175/1520-0477(1988)069 < 0148:goalea > 2.0.co;2.

Eichenlaub, V. L. (1970), Lake effect snowfall to the lee of the Great Lakes: Its role in Michigan, *Bull. Am. Meteorol. Soc.*, *51*, 403–412.

Enomoto, T., A. Kuwano-Yoshida, N. Komori, and W. Ohfuchi (2008), Description of AFES2: Improvements for high-resolution and coupled simulations, in *High Resolution Numerical Modelling of the Atmosphere and Ocean*, edited by K. Hamilton and W. Ohfuchi, chap. 5, pp. 77–97, Springer, New York.

Enomoto, T., T. Miyoshi, Q. Moteki, J. Inoue, M. Hattori, A. Kuwano-Yoshida, N. Komori, and S. Yamane (2013), Observing-system research and ensemble data assimilation at JAMSTEC, in *Data Assimilation for Atmospheric, Oceanic and Hydrologic Applications*, vol. II, edited by S. K. Park and L. Xu, chap. 21, pp. 509–526, Springer, Berlin.

Francis, J. A., and S. J. Vavrus (2012), Evidence linking Arctic amplification to extreme weather in mid-latitudes, *Geophys. Res. Lett.*, *39*, L06801, doi:10.1029/2012GL051000.

Francis, J. A., and S. J. Vavrus (2015), Evidence for a wavier jet stream in response to rapid Arctic warming, *Environ. Res. Lett.*, *10*, 014005.

Graf, H.-F., and D. Zanchettin (2012), Central Pacific El Nin~o, the "subtropical bridge," and Eurasian climate, *J. Geophys. Res.*, *117*, D01102, doi:10.1029/2011JD016493.

Granskog, M. A., P. Assmy, S. Gerland, G. Spreen, H. Steen, and L. H. Smedsrud (2016), Arctic research on thin ice: Consequences of Arctic sea ice loss, *Eos Trans. AGU*, *97*, 22–26, doi:10.1029/2016EO044097.

Honda, M., J. Inoue, and S. Yamane (2009), Influence of low Arctic sea-ice minima on anomalously cold Eurasian winters, *Geophys. Res. Lett.*, *36*, L08707, doi:10.1029/2008GL037079.

Hotta, D. (2014), Proactive quality control based on ensemble forecast sensitivity to observations, PhD dissertation, Univ. of Md., College Park. [Available at https://www.atmos.umd.edu/~ekalnay/dissertations/Hotta-Dissertation-revised-after-defense-2.pdf.]

Hunt, B. R., E. J. Kostelich, and I. Szunyogh (2007), Efficient data assimilation for spatiotemporal chaos: A local ensemble transform Kalman filter, *Physica D*, *230*, 112–126, doi:10.1016/j.physd.2006.11.008.

Inoue, J., M. Kawashima, Y. Fujiyoshi, and M. Yoshizaki (2005), Aircraft observations of air-mass modification upstream of the Sea of Japan during cold-air outbreaks, *J. Meteorol. Soc. Jpn.*, *83*, 189–200.

Inoue, J., T. Enomoto, T. Miyoshi, and S. Yamane (2009), Impact of observations from Arctic drifting buoys on the reanalysis of surface fields, *Geophys. Res. Lett.*, *36*, L08501, doi:10.1029/2009GL037380.

Inoue, J., M. E. Hori, T. Enomoto, and T. Kikuchi (2011), Intercomparison of surface heat transfer near the Arctic marginal ice zone for multiple reanalyses: A case study of September 2009, *Sci. Online Lett. Atmos.*, *7*, 57–60.

Inoue, J., M. E. Hori, and K. Takaya (2012), The role of Barents Sea ice in the wintertime cyclone track and emergence of a warm-Arctic cold-Siberian anomaly, *J. Clim.*, *25*, 2561–2568, doi:10.1175/JCLI-D-11-00449.1.

Inoue, J., T. Enomoto, and M. E. Hori (2013), The impact of radiosonde data over the ice-free Arctic Ocean on the atmospheric circulation in the Northern Hemisphere, *Geophys. Res. Lett.*, *40*, 864–869, doi:10.1002/grl.50207.

Inoue, J., A. Yamazaki, J. Ono, K. Dethloff, M. Maturilli, R. Neuber, P. Edwards, and H. Yamaguchi (2015), Additional Arctic observations improve weather and sea-ice forecasts for the Northern Sea Route, *Sci. Rep.*, *5*, 16868, doi:10.1038/srep16868.

Iwasaki, T., T. Shoji, Y. Kanno, M. Sawada, M. Ujiie, and K. Takaya (2014), Isentropic analysis of polar cold airmass streams in the northern hemispheric winter, *J. Atmos. Sci.*, *71*, 2230–2243.

Jung, T., and M. Leutbecher (2007), Performance of the ECMWF forecasting system in the Arctic during winter, *Q. J. R. Meteorol. Soc.*, *133*, 1327–1340.

Jung, T., and M. Matsueda (2014), Verification of global numerical weather forecasting systems in polar regions using TIGGE data, *Q. J. R. Meteorol. Soc.*, *142*, 574–582.

Jung, T., M. A. Kasper, T. Semmler, and S. Serrar (2014), Arctic influence on subseasonal midlatitude prediction, *Geophys. Res. Lett.*, *41*, 3676–3680, doi:10.1002/2014GL059961.

Jung, T., et al. (2016), Advancing polar prediction capabilities on daily to seasonal time scales, *Bull. Am. Meteorol. Soc.*, doi:10.1175/BAMS-D-14-00246.1, in press.

Kalnay, E., Y. Ota, T. Miyoshi, and J. Liu (2012), A simpler formulation of forecast sensitivity to observations: Application to ensemble Kalman filters, *Tellus, Ser. A*, *64*, 18462.

Kim, B.-M., S.-W. Son, S.-K. Min, J.-H. Jeong, S.-J. Kim, X. Zhang, T. Shin, and J.-H. Yoon (2014), Weakening of the stratospheric polar vortex by Arctic sea-ice loss, *Nat. Commun.*, *5*, 4646, doi:10.1038/ncomms5646.

Konrad, C. E., II (1996), Relationships between the intensity of cold air outbreaks and the evolution of synoptic and planetary-scale features over North America, *Mon. Weather Rev.*, *124*, 1067–1083.

Kristjánsson, J. E. et al. (2011), The Norwegian IPY-THOPEX: Polar lows and Arctic fronts during the 2008 Andøya Campaign, *Bull. Am. Meteorol. Soc.*, *92*, 1443–1466.

Kug, J.-S., J.-H. Jeong, Y.-S. Jang, B.-M. Kim, C. K. Folland, S.-K. Min, and S.-W. Son (2015), Two distinct influences of Arctic warming on cold winters over North America and East Asia, *Nat. Geosci.*, *8*, 759–762, doi:10.1038/ngeo2517.

Lee, M.-Y., C.-C. Hong, and H.-H. Hsu (2015), Compounding effects of warm sea surface temperature and reduced sea ice on the extreme circulation over the extratropical North Pacific and North America during the 2013–2014 boreal winter, *Geophys. Res. Lett.*, *42*, 1612–1618, doi:10.1002/2014GL062956.

Lenschow, D. H., and E. M. Agee (1976), Preliminary results from the air mass transformation experiment (AMTEX), *Bull. Am. Meteorol. Soc.*, *57*, 1346–1355.

Liu, J., J. A. Curry, H. Wang, M. Song, and R. M. Horton (2012), Impact of declining Arctic sea ice on winter snowfall, *Proc. Natl. Acad. Sci. U. S. A.*, *109*, 4074–4079.

Luo, D., Y. Xiao, Y. Yao, A. Dai, I. Simmonds, and C. L. E. Franzke (2016), Impact of Ural blocking on winter warm arctic-cold Eurasian anomalies. Part I: Blocking-induced amplification, *J. Clim.*, doi:10.1175/JCLI-D-15-0611.1, in press.

Miyoshi, T., and S. Yamane (2007), Local ensemble transform Kalman filtering with an AGCM at a T159/L48 resolution, *Mon. Weather Rev.*, *135*, 3841–3861, doi:10.1175/2007MWR1873.1.

Mori, M., M. Watanabe, H. Shiogama, J. Inoue, and M. Kimoto (2014), Robust Arctic sea-ice influence on the frequent Eurasian cold winters in past decades, *Nat. Geosci.*, *7*, 869–873, doi:10.1038/ngeo2277.

Nakamura, T., K. Yamazaki, K. Iwamoto, M. Honda, Y. Miyoshi, Y. Ogawa, and J. Ukita (2015), A negative phase shift of the winter AO/NAO due to the recent Arctic sea-ice reduction in late autumn, *J. Geophys. Res. Atmos.*, *120*, 3209–3227, doi:10.1002/2014JD022848.

Nakanowatari, T., K. Sato, and J. Inoue (2014), Predictability of the Barents Sea ice in early winter: Remote effects of oceanic and atmospheric thermal conditions from the North Atlantic, *J. Clim.*, *27*, 8884–8901.

Nakanowatari, T., J. Inoue, K. Sato, and T. Kikuchi (2015), Summertime atmosphere-ocean preconditionings for the Bering Sea ice retreat and the following severe winters in North America, *Environ. Res. Lett.*, *10*, 094023, doi:10.1088/1748-9326/10/9/094023.

Ninomiya, K. (1975), Large-scale heat and moisture budgets during the air-mass transformation over the East China Sea during AMTEX'74, *J. Meteorol. Soc. Jpn.*, *53*, 285–303.

Ohfuchi, W., H. Nakamura, M. K. Yoshioka, T. Enomoto, K. Takaya, X. Peng, S. Yamane, T. Nishimura, Y. Kurihara, and K. Ninomiya (2004), 10-km mesh meso-scale resolving simulations of the global atmosphere on the Earth Simulator—Preliminary outcomes of AFES (AGCM for the Earth Simulator), *J. Earth Simul.*, *1*, 8–34.

Ono, J., J. Inoue, A. Yamazaki, K. Dethloff, and H. Yamaguchi (2016), The impact of radiosonde data on forecasting sea-ice distribution along the Northern Sea Route during an extremely developed cyclone, *J. Adv. Model. Earth Syst.*, *8*, 292–303, doi:10.1002/2015MS000552.

Ota, Y., J. C. Derber, E. Kalnay, and T. Mioshi (2013) Ensemble-based observation impact estimates using the NCEP GFS, *Tellus, Ser. A*, *65*, 20038.

Overland, J. E. (2016), A difficult Arctic science issue: Midlatitude weather linkages, *Polar Sci.*, *10*, 210–2016, doi:10.1016/j.polar.2016.04.011.

Overland, J. E., J. Francis, R. Hall, E. Hanna, S.-J. Kim, and T. Vihma (2015), The melting Arctic and mid-latitude weather patterns: Are they connected?, *J. Clim.*, *28*(20), 7917–7932, doi:10.1175/JCLI-D-14-00822.1.

Reynolds, R. W., T. M. Smith, C. Liu, D. B. Chelton, K. S. Casey, and M. G. Schlax (2007), Daily high-resolution-blended analyses for sea surface temperature, *J. Clim.*, *20*, 5473–5496, doi:10.1175/2007JCLI1824.1.

Santorelli, A. (2015), Southern Plains to Mid-Atlantic Winter Storm. [Available at http://www.wpc.ncep.noaa.gov/winter_storm_summaries/event_reviews/2015/SouthernPlains_MidAtlantic_WinterStorm_Feb2015.pdf, Natl. Oceanic and Atmos. Admin., Weather Predict. Cent.]

Sato, K., J. Inoue, and M. Watanabe (2014), Influence of the Gulf Stream on the Barents Sea ice retreat and Eurasian coldness during early winter, *Environ. Res. Lett.*, *9*, 084009, doi:10.1088/1748-9326/9/8/084009.

Simmonds, I. (2015), Comparing and contrasting the behaviour of Arctic and Antarctic sea ice over the 35-year period 1979-2013, *Ann. Glaciol.*, *56*(69), 18–28.

Simmonds, I., and P. D. Govekar (2014), What are the physical links between Arctic sea ice loss and Eurasian winter climate?, *Environ. Res. Lett.*, *9*, 101003, doi:10.1088/1748-9326/9/10/101003.

Vihma, T. (2014), Effects of Arctic sea ice decline on weather and climate: a review, *Surv. Geophys.*, *35*, 1175–1214.

Yamazaki, A., J. Inoue, K. Dethloff, M. Maturilli, and G. König-Langlo (2015), Impact of radiosonde observations on forecasting summertime Arctic cyclone formation, *J. Geophys. Res. Atmos.*, *120*, 3249–3273, doi:10.1002/2014JD022925.

Yoshizaki, M., T. Kato, H. Eito, S. Hayashi, and W.-K Tao (2004), An overview of the field experiment "Winter Mesoscale Convective Systems (MCSs) over the Japan Sea in 2001," and comparisons of the cold-air outbreak case (14 January) between analysis and a non-hydrostatic cloud-resolving model,. *J. Meteorol. Soc. Jpn.*, *82*, 1365–1387.